J. Fluid Mech. (1995), *vol.* 292, *pp.* 333–358

Stratified circular Couette flow: instability and flow regimes

By B. M. BOUBNOV†, E. B. GLEDZER† AND E. J. HOPFINGER

LEGI/IMG, CNRS–UJF–INPG, B.P. 53X, 38041 Grenoble Cedex, France

(Received 22 June 1994 and in revised form 30 January 1995)

The stability conditions of the flow between two concentric cylinders with the inner one rotating (circular Couette flow) have been investigated experimentally and theoretically for a fluid with axial, stable linear density stratification. The behaviour of the flow, therefore, depends on the Froude number $Fr = \Omega/N$ (where Ω is the angular velocity of the inner cylinder and N is the buoyancy frequency of the fluid) in addition to the Reynolds number and the non-dimensional gap width ϵ, here equal to 0.275.

Experiments show that stratification has a stabilizing effect on the flow with the critical Reynolds number depending on N, in agreement with linear stability theory. The selected, most amplified, vertical wavelength at onset of instability is reduced by the stratification effect and is for the geometry considered only about half the gap width. Furthermore, the observed instability is non-axisymmetric. The resulting vortex motion causes some mixing and this leads to layer formation, clearly visible on shadowgraph images, with the height of the layer being determined by the vertical vortex size. This regime of vertically reduced vortex size is referred to as the S-regime.

For larger Reynolds and Froude numbers the role of stratification decreases and the most amplified vertical wavelength is determined by the gap width, giving rise to the usual Taylor vortices (we call this the T-regime). The layers which emerge are determined by these vortices. For relatively small Reynolds number when $Fr \approx 1$ the Taylor vortices are stable and the layers have a height h equal to the gap width; for larger Reynolds number or $Fr \approx 2$ the Taylor vortices interact in pairs (compacted Taylor vortices, regime CT) and layers of twice the gap width are predominant. Stratification inhibits the azimuthal wavy vortex flow observed in homogeneous fluid. By further increasing the Reynolds number, turbulent motions appear with Taylor vortices superimposed like in non-stratified fluid.

The theoretical analysis is based on a linear stability consideration of the axisymmetric problem. This gives bounds of instability in the parameter space (Ω, N) for given vertical and radial wavenumbers. These bounds are in qualitative agreement with experiments. The possibility of oscillatory-type instability (overstability) observed experimentally is also discussed.

1. Introduction

One of the classical hydrodynamic stability problems of major importance is the flow of fluid confined to the annulus between concentric, rotating cylinders. Since the pioneering works by Couette (1890) and Taylor (1923) a very large number of

† Permanent address: Institute of Atmospheric Physics, 109017, Moscow, Russia.

experimental and theoretical studies have considered different aspects of instability and transitions of this flow configuration (see for instance Di Prima & Swinney 1981; Andereck, Liu & Swinney 1986; Chossat & Iooss 1994).Various modifications of this problem have also received considerable attention and these include the influence of axial flow (Gravas & Martin 1978; Lueptov, Docter & Min 1992), unsteadiness of the rotation rate (Cooper *et al.* 1985) and the effect of radial temperature or density variations with and without an axial gravitational field (Snyder & Karlsson 1964; Yao & Rogers 1989; Kubotani *et al.* 1989; Ali & Weidman 1990).

In the simplest case of Couette–Taylor flow, with only the inner cylinder rotating, a variety of different regimes are observed: Taylor vortices, wavy vortices, modulated wavy vortices, turbulent Taylor vortices. When additional effects are included (Coriolis force, velocity shear, radial density stratification etc.) significant changes in the stability occur and the flow states reveal a rich variety of phenomena (Andereck *et al.* 1986, for instance found more than fifteen principal flow regimes between independently rotating cylinders in homogeneous fluid). Surprisingly, the case of the interaction of centrifugal and buoyancy forces, namely circular Couette flow with axial density stratification, has not received much attention. The only previous theoretical considerations of this configuration are by Thorpe (1966). He investigated the analogy of this problem with rotating Bénard convection (mentioned by Chandrasekhar 1961, see also Veronis 1970); he concluded that stable stratification delays the occurrence of rolls in the azimuthal direction and reduces their height.

It has been argued by Hua (see Hua & Moore 1994) that centrifugal-type instability may be at the origin of equatorial jet formation and this motivated us to study the stratified Couette–Taylor problem in more detail. In the equatorial region the potential vorticity is negative and rotational instability of the zonal flow is thus possible, leading to rolls oriented latitudinally. Such rolls would modify the velocity of the equatorial undercurrent in a jet-like fashion (more or less sinusoidal velocity variation with depth). Stratification flattens the rolls in the vertical.

In the present study the simplest case of linear stratification and with only the inner cylinder rotating has been considered experimentally and theoretically. The aim was to determine the dependence on stratification of the instability and the further transitions in flow structure and to know by how much the vertical size of the rolls is reduced by stratification. It is shown that density stratification has a strong effect on the onset of instability and the resulting vortex structures. The vortices cause mixing by overturning and hence the formation of layers of height equal to the vertical vortex size. It is noteworthy that the layer height changes in a discrete manner from less than the gap width to one and then to twice to gap width.

The main non-dimensional parameters of the problem are the usual Reynolds number $Re = \Omega a(b-a)/\nu$ (see e.g. Andereck *et al.* 1986), and the non-dimensional gap width $\epsilon = b/a-1$ (a and b are the radii of inner and outer cylinders respectively, Ω the angular velocity of the inner cylinder, and ν the kinematic viscosity). The stratification is expressed by the Brunt–Väisälä or buoyancy frequency $N = \left(-(g/\rho)\partial\rho/\partial z\right)^{1/2}$ (where ρ is the density and g the gravitational acceleration), and this introduces an additional non-dimensional parameter which is the Froude number $Fr = \Omega/N$.

In §2 are presented the experimental apparatus and procedure. Section 3 contains the main experimental results, concerning the instability and other flow regimes; the dependency of onset of instability on the main non-dimensional parameters and also

the non-axisymmetric structure which arises after onset of instability are discussed. In §4 the results of linear stability theory for the small-gap approximation are compared with experiments. Further discussion and conclusions are presented in §5.

2. Experimental apparatus and procedure

The experimental installation for circular Couette flow in stratified fluid is similar to those which are used for studying Couette–Taylor flow in homogeneous fluid. It consists of long coaxial transparent Plexiglas cylinders with the outer cylinder, the bottom and surface being at rest and the inner cylinder rotating with constant angular velocity Ω. The outer cylinder has an inner radius of $b = 51$ mm, and the inner cylinder has an outer radius $a = 40$ mm, giving a non-dimensional gap width $\epsilon = 0.275$. This ϵ is sufficiently small for interpreting the results in the context of the small-gap approximation theory (see Di Prima & Swinney 1981) and the gap is still sufficiently large for observing details of the vortex and layer structure. The length of the cylinder is $L = 573$ mm, or $\Gamma = L/(b-a) = 52$. In most experiments the gap was filled completely with linearly stratified salt solution and the upper boundary was rigid; only in experiments with large density gradient, when $N > 1.5$ s^{-1} (the numerical values of Ω and N are throughout the paper in rad s^{-1}), was the upper boundary free, because in order to reach this value of N it was necessary to fill the space between the cylinders to a depth less than L. In our experiments stable density stratification inhibits propagation of disturbances from the top and bottom boundaries to the fluid interior and there is no influence of boundary conditions on the flow regimes (which would not be the case in non-stratified fluid, where end boundary conditions are very important in the onset of instability when Γ is not large).

The linear stratification was accomplished by using a salt solution and the standard 'double-bucket' filling method (Oster 1965). The time of filling was of the order of two hours. Normally, stratification measurements were made by taking samples at four different depths or more. The linearity of the density profile was also verified with the help of shadowgraphs, in which the outer surface of the inner cylinder appears as a straight line inclined at some angle to the vertical, with the inclination being proportional to the Brunt–Väisälä freguency N. The deviations of the density profiles from linearity in the main part of the fluid column ($0.1 < z/L < 0.9$, where z is the vertical coordinate) were less then 5% (determined from variations between the samples taken). The value of N was changed in the limits $0.35 < N < 1.78$ s^{-1}. The change in kinematic viscosity due to the change in salinity is 10% when N change from 0.4 to 1.7 and this change was accounted for when calculating Reynolds numbers.

In order to reduce optical distortsions due to the curvature of the cylinders, the apparatus was placed in a large square box filled with water (there is also water in the inner cylinder). This also helped to keep the temperature uniform. For the flow visualizations two different and complementary techniques were used: a shadowgraph technique, sensitive to the second derivative of density which allows the horizontally averaged density structures to be seen, and particle streak line methods to visualize the vortex motion. Aluminium powder and kalliroscope particles were used in this case. The aluminium particles are almost isotropic and move with the fluid and show the motions in the vortices, while plane kalliroscope flakes outline primarily the vortex structure of the flow.

The inner cylinder was rotated with an angular velocity Ω maintained constant within 1% and its value could be changed continuously from 0.1 to 3.7 s^{-1}. Steady rotation of the inner cylinder was reached in less than 2 s after switch-on and stable,

steady-state azimuthal fluid motion was established, on average, in a time of about 10 min. The time for observable (on shadowgraph) instability of the zonal, axisymmetric flow depends how close the rotation rate is to critical conditions.

Two experimental procedures have been used: one starts with the fluid at rest and suddenly setting the angular velocity Ω to the desired supercritical value and the other increases Ω from one value to another. The later incremental procedure (small increments) is necessary for the determination of the neutral stability curve. The other flow states were obtained with the former method of setting Ω to the desired supercritical value. After an experiment with one rotation rate Ω was finished and the layers formed were allowed to diffuse, the linearity of the main stratification was checked and a new experiment could be started.

3. Experimental results

3.1. *Flow regimes*

The diagram of observed flow regimes in the (Ω,N) parameter space is shown in figure 1. Here, we briefly describe the main regimes and transitions between them with more quantitative details being given later. In the determination of the neutral stability curve the rotation rate Ω was increased by small increments until the critical value of $\Omega_c(N)$ for the onset of instability was reached. All the other flow states and bounds shown in figure 1 for $\Omega > \Omega_c(N)$ were obtained by starting with the fluid at rest and by setting Ω to the desired supercritical value. For $\Omega < \Omega_c(N)$ the flow has only an azimuthal component of velocity (circular Couette flow) with no changes in the density field along the vertical axis (regime A, figure 1). This steady flow arises shortly after (about 10 min) the start of rotation of the inner cylinder. For $\Omega \geqslant \Omega_c(N)$ on the other hand, the shadowgraph images indicated vertical variations in density with the appearance of easily identifiable layers of nearly equal height. By this means it was possible to determine Ω_c as a function of N. Note that because of the gradient in kinematic viscosity ν, caused by the salinity gradient, instability at large N was always first observed near the top of the cylinder where ν is less. The critical value of Ω was always determined from onset observed in the central part. In the neutral case of $N = 0$ the critical value of Ω (needed for comparison with the results of other studies and to test the theoretical value) was determined from the onset of the motion of particles suspended in the fluid. For the present experimental conditions $\Omega_c(0) \simeq 0.21$ s^{-1}, giving a Reynolds number $Re_c(0) = \Omega_c a(b-a)/\nu \simeq 90$. This is in agreement with the expected value of 0.208 s^{-1} (Di Prima & Swinney 1981). For $N = 0$ the instability of circular Couette flow gives rise to axisymmetric Taylor vortices of vertical size equal to the width of the gap.

For stratified Couette flow when N is large enough ($N > 0.4$) and Ω just above $\Omega_c(N)$, the first layers visible on the shadowgraph are of height h approximately equal to one half of the gap width giving $n_l = h/(b-a) \approx \frac{1}{2}$ (n_l is the non-dimensional layer height or layer height factor). These layers with $n_l \approx \frac{1}{2}$ are observed in the stratification-dominated flow regime, called the S-regime. With increasing Ω, the usual Taylor vortices are also appearing. Steady Taylor vortices indicated by $n_l = 1$ are observed for values of Ω and N lying in region T of figure 1. Between regions S and T there exists a transition region ST in which both regimes with $n_l \approx 1/2$ and $n_l = 1$ are observed. When we move to larger Ω (for the same N) the Taylor vortices become more and more unsteady and vortices begin to interact in pairs. As a result, instead of wavy vortices, observed in homogeneous fluid for large Ω (see Andereck *et al.* 1986 and

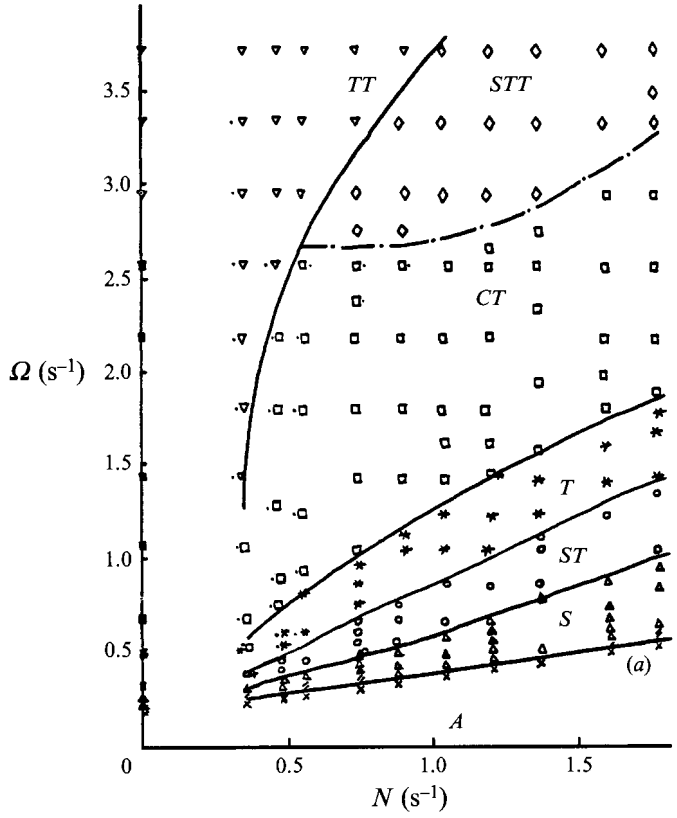

FIGURE 1. Experimentally determined instability and flow regimes for stratified circular Couette flow ($\epsilon = 0.275$): ×, (A-regime) stable azimuthal flow; △, (S) stratification-dominated flow with $n_l \approx 1/2$; ○, (ST) transition between $n_l \approx 1/2$ and $n_l = 1$, both exist simultaneously; *, (T) Taylor vortices $n_l = 1$; □, (CT) compacted Taylor vortices with $n_l = 2$; ◇, (STT) turbulent motion with $n_l = 2$ and observable layers after stop; ▽, (TT) turbulent mixing without layers after stop; /, weak vortices with local mixing and partial interfaces, $n = 1$. For $N = 0$: ▲, Taylor vortices; ■, wavy Taylor vortices. The lines drawn in the figure indicate the approximate boundaries between the different regimes.

square black symbols in figure 1), layers of $n_l \approx 2$ arise with two closely spaced Taylor vortices inside; this is the region CT in figure 1 with CT standing for Taylor vortices compacted in pairs . Shadowgraph images of the different layers corresponding to regimes S, ST, T and CT are shown in figure 2 for $N = 1.2\ \mathrm{s}^{-1}$. From figure 1 one can see that onset of instability and the boundaries between the main regimes are characterized by a Froude number Ω/N rather than by Reynolds number.

By further increasing Ω, more complicated turbulent interactions between the vortices may be observed (region STT in figure 1). For small N the regime of transition to strong turbulent mixing also exists (regime TT). The difference between regimes STT and TT is that in the stratification-affected turbulent regime (STT) layers are visible after stopping the rotation, whereas this is not the case in the TT-regime. It should also be remarked that for all regular regimes the layer structure formed is conserved for a long time after stopping the rotation of the cylinder (for example in regime T layers remained visible up to half an hour).

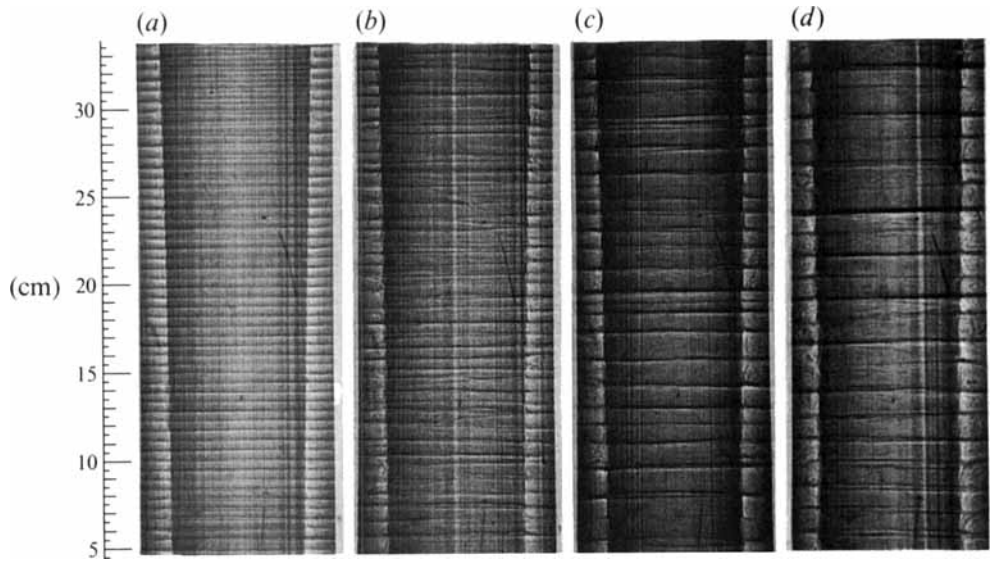

FIGURE 2. Shadowgraph visualizations of the change in layer height as a function of angular velocity Ω of the inner cylinder, $N = 1.2\ \mathrm{s}^{-1}$. (*a*) $\Omega = 0.6\ \mathrm{s}^{-1}, h \approx (b-a)/2$ (*S*-regime); (*b*) $\Omega = 0.9\ \mathrm{s}^{-1}$, transition from $h \approx (b-a)/2$ to $h \approx (b-a)$, (*ST*-regime); (*c*) $\Omega = 1.2\ \mathrm{s}^{-1}, h \approx (b-a)$ (*T*-regime); (*d*) $\Omega = 2.4\ \mathrm{s}^{-1}$, $h \approx 2(b-a)$ (*CT*-regime).

3.2. *Onset of instability*

Usually, instability of stratified, circular Couette flow is manifest by the appearance of (regular) density layers on the shadowgraph images. In the range $\Omega/N < 0.5$ the height h of these layers strongly depends on the buoyancy frequency N or more precisely on the Froude number Ω/N. The value of h varied between 5.5 mm and 8.5 mm (for a gap width $d = b - a = 11$ mm). From figure 3 it is seen that the dependency of the layer height on Froude number may be expressed by the empirical formula

$$n_l = C_1 \frac{\Omega}{N}, \quad C_1 \approx 1.38 \tag{3.1}$$

indicated by the solid line in figure 3.

The vortices responsible for the layer formation of height h have a vertical wavelength $\lambda = 2h$ giving a wavelength factor defined as $n = \lambda/2d$ equal to n_l. At onset of instability the vortices are counter-rotating in pairs and the vortex structure is asymmetric. To prove the asymmetry we introduced kalliroscope flakes in the fluid and used a light sheet (about 1 cm thick) parallel to the axis of rotation. The images obtained for flow regime *S* ($\Omega = 0.55\ \mathrm{s}^{-1}$, $N = 1.1\ \mathrm{s}^{-1}$) are shown in figure 4. These images indicate a periodic change (the picture of the flow pattern corresponds to section 'B-B' in the top view of the gap between the cylinders shown in figure 5). The horizontal line in figure 4 is at a fixed position with respect to the outer cylinder or the non-rotating coordinate system and it is seen that the positions of the white maxima in figures 4(*a*) and 4(*c*) are opposite. Figures 4(*b*) and 4(*d*) show the intermediate states. Figure 4 indicates an oscillatory behaviour but observations in one section are no proof of non-axisymmetry. We also made simultaneous visualizations in a diametrically opposite section which demonstrated an asymmetry. It was, however, not possible to decide whether the asymmetry is of mode $m = 1$ or 2.

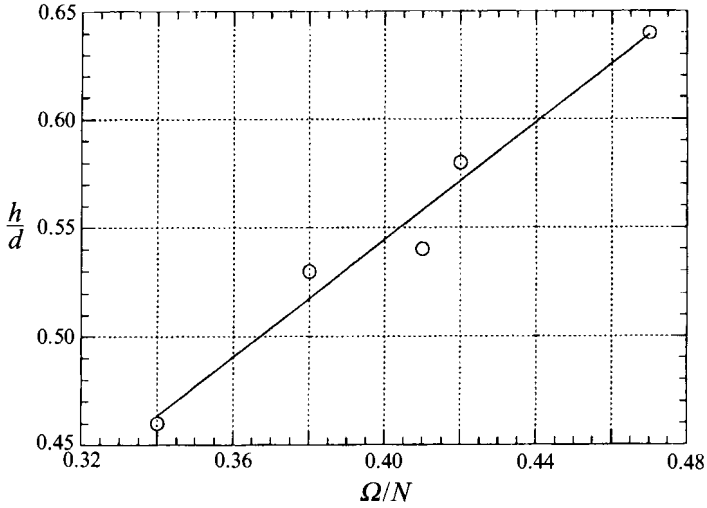

FIGURE 3. Dependence of layer thickness on Ω/N in the S-regime for $\Omega/N < 0.5$. The solid line corresponds to $n_l = 1.38\ \Omega/N$.

Non-axisymmetric motions at onset of instability of the azimuthal flow can be explained by considering that when stratification is important the vortices are smaller than the gap width and can, therefore, move in the horizontal plane. Since adjacent vortices are counter-rotating, vortex pairs at one position tend to move away from the inner cylinder and at another position toward it. Such a row of vortices is likely not to be stable and may give rise to oscillations and to a non-axisymmetric vortex configuration (a stable axisymmetric state would require vortices which are elongated in the horizontal direction to fill the gap). As a result we can have wavy motions in the azimuthal direction with wavenumber m. In our particular case m may be either 1 or 2 as indicated in figure 5.

The time it takes from the start of cylinder rotation until layers become visible depends on how close Ω is to the critical rotation rate. Very close to critical conditions ($\Omega = 1.1\ \Omega_c$) a layered density structure becomes visible after about 20 rotation periods. In these conditions the layers are, however, not very steady (interfaces appear and disappear) probably because there is very little mixing. For conditions shown in figure 2(a), corresponding to about $1.4\ \Omega_c$, there is more intensive mixing and very stable layers are established in about 30 rotation periods. On shadowgraph images such as shown in figure 2(a), the density interfaces (dark lines) remain clearly at a fixed position. The corresponding vortex structures in the layers between the interfaces are shown for the S-regime schematically in figure 5, consistent with the images of figure 4(a–d). The vortex structure in this regime visualized in a diametrical section 'A-A', by kalliroscopic particles, is shown in figure 6(a) and by aluminium particles in figure 7(a). In figure 7(a) the apparent wavy axial flow reflects the flow induced by the vortices.

The Froude number $Fr = \Omega/N$ is a measure of the relative importance of centrifugal to buoyancy forces. For the case when $Fr >> 1$ the centrifugal force dominates the motion and the influence of stratification is a small additional effect. This is reflected in the flow in regimes TT and STT where the influence of stratification is negligible. The opposite is the case in regime S when the Froude number is less then 1. In this case stratification controls the size of the

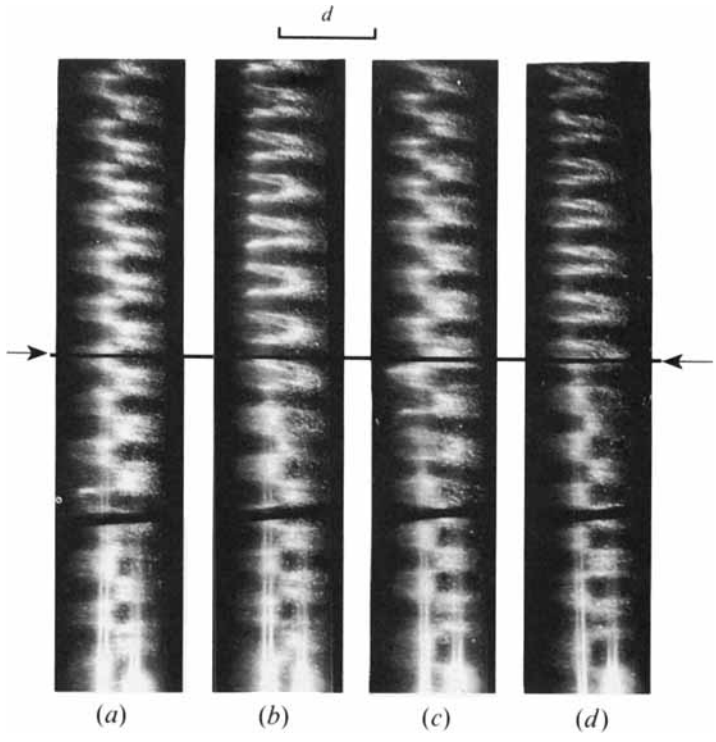

FIGURE 4. Kalliroscope particle visualizations for periodic S-regime, $N = 1.1\ \mathrm{s}^{-1}, \Omega = 0.55\ \mathrm{s}^{-1}$ ($\Omega = 1.3\ \Omega_c$): (*a*) $t = 0$, (*b*) $t = 6$ s, (*c*) $t = 12$ s, (*d*) $t = 19$ s.

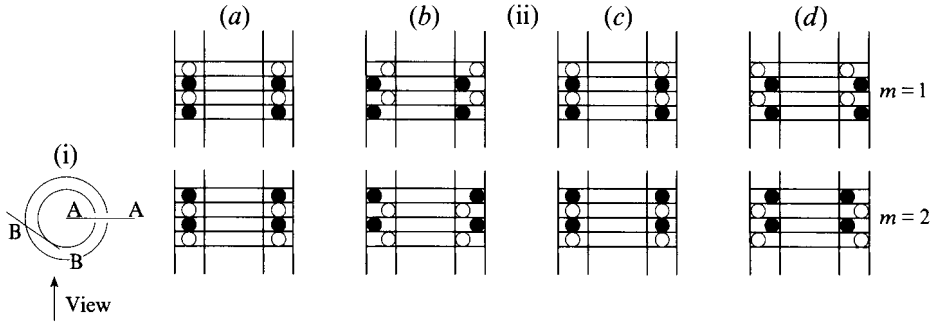

FIGURE 5. Schematic top view and sections of the gap between the cylinders. (i) Top view with light sheet orientations B-B and A-A; (ii) lateral cross-section views of the toroidal non-axisymmetric vortices in the gap for the S-regime: $m = 1$ (upper part) and $m = 2$ (lower part). For view (ii) the times are: (*a*) $t = 0$; (*b*) $t = T_1/4$; (*c*) $t = T_1/2$; (*d*) $t = 3T_1/4$, where T_1 is the period of oscillation. In the case shown in figure 4, $T_1 = 38$ s.

vortex structure. For some Froude numbers onset of instability occurs via weak vortex elements of height $h \approx d/2$ which cause only weak, local mixing over a height $h \approx d$. The interfaces visible on the shadowgraphs span only a fraction of the circumference. The whole pattern rotates with constant velocity. The existence of these vortices, marked by inclined dashes (/) on figure 1, may be a result of resonant internal wave–vortex interactions; all of these points are near the points of intersection of the stability curve (*a*) and lines $Fr = 1, 1/2$ and $1/3$.

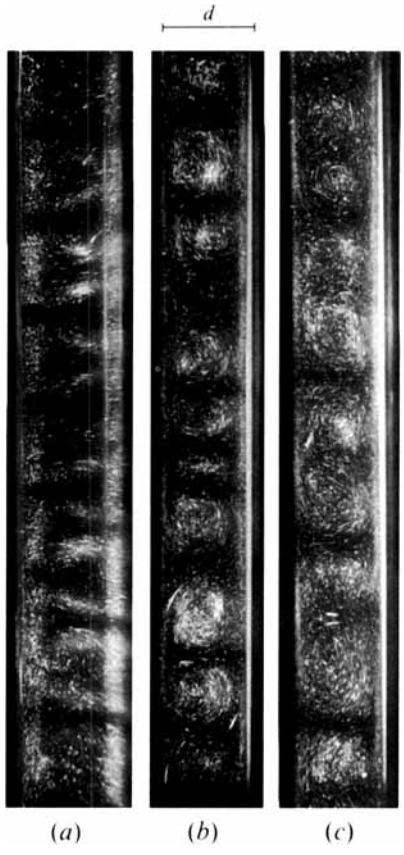

FIGURE 6. Kalliroscope particle visualizations (short time exposure images) for different regimes ($N = 0.92$ s^{-1}): (*a*) *S*-regime with $\Omega = 0.43$ s^{-1}; (*b*) *T*-regime with $\Omega = 0.92$ s^{-1}; (*c*) *CT*-regime with $\Omega = 1.82$ s^{-1}.

3.3. *The T-regime* ($n_l = 1$)

When the Froude number is near unity or larger, the centrifugal effects dominate the instability mode and Taylor vortices appear. These vortices are toroidal and are of equal vertical and horizontal size and are equal to the gap between the cylinders. The corresponding vertical wavelength is $\lambda = 2d$ giving $n = 1$. Taylor vortices exist in the Ω, N parameter space indicated by T in figure 1 and the corresponding layer height factor is $n_l = 1$ (figure 2*c*). The time required to reach a steady state is about 30 rotation periods after starting the inner cylinder rotation. Although at some fluid depths vortices are formed in less than 5 rotation periods, a steady regular system of vortices over nearly the whole fluid depth was reaches only after some interaction.

Examples of Taylor vortices visualized by kalliroscopic particles and aluminium powder are presented respectively in figures 6(*b*), 7(*b*), showing fairly regular, well-developed vortices. Neighbouring vortices have opposite rotation as is the case for the usual Taylor vortices.

3.4. *Compacted vortices, CT-regime* ($n_l = 2$)

The main difference between the regimes with $n_l = 1$ and $n_l = 2$ is that the interfaces separating layers (dark-bright lines on shadowgraph images) are of approximately equal intensity in the *T*-regime with $n_l = 1$ (figure 2*c*). In the *CT*-regime on the other

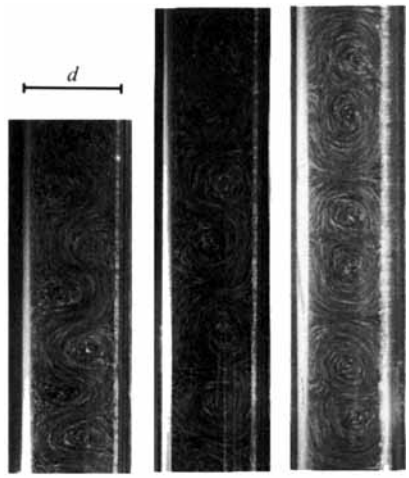

FIGURE 7. Vortex structures in the different regimes (visualization by aluminium particles using long time exposure; $N = 1.20\ \mathrm{s}^{-1}$): (*a*) *S*-regime with $\Omega = 0.6\ \mathrm{s}^{-1}$, (*b*) *T*-regime with $\Omega = 1.2\ \mathrm{s}^{-1}$, (*c*) *CT*-regime with $\Omega = 2.4\ \mathrm{s}^{-1}$.

hand the intensity of every second interface is weaker (figure 2*d*). This effect is even better displayed when the rotation of the inner cylinder is stopped and after some time only the stronger interfaces separating layers with $n_l = 2$ remain. At later times these disappear, also by diffusion.

In this regime, Taylor vortices are also the main structures, but these interact in pairs (are compacted in pairs) and a weaker mode $n = 2$ is present. The interaction is such that the centres of neighbouring vortices sometimes disappear and re-emerged, and it is also possible that one of the interacting vortices may even change its sense of rotation. In figure 6(*c*) the interaction in pairs and some presence of mode $n = 2$ is indicated by the absence of kalliroscope particles outside the compact vortex pairs with mixing inside the pairs. The particle streak pictures (figure 7*c*) show, in addition to the two compacted Taylor vortices, a flow over a height equal to 2*d*. These results further support the interaction between the main mode $n = 1$ and a mode $n = 2$.

3.5. *Transition and turbulent regimes*

The transition and turbulent regimes are characterized by the absence of steady layers. Transition regimes are observed in the region between regimes with different n_l, in particular between $n_l \approx 1/2$ and $n_l = 1$ and also for large values of Ω. The transition regimes between steady states exhibit complex internal wave motions near the interfaces. Some examples of these transition regimes are shown in figure 8. Figure 8(*b*) shows the transition regime *ST* lying between the *S*-regime with steady layers (figure 8*a*) and the *T*-regime; internal waves propagate along the interfaces shown in figure 8(*b*). In the nearly turbulent regime, regions with random interfaces are adjacent to regions of more stable layers of $n_l = 2$ (figure 8*c*). Their positions change with time also in a random fashion. In the turbulent regime it is thought that stratification has only a very weak effect on the dynamics with the internal waves taking only a small fraction of the energy.

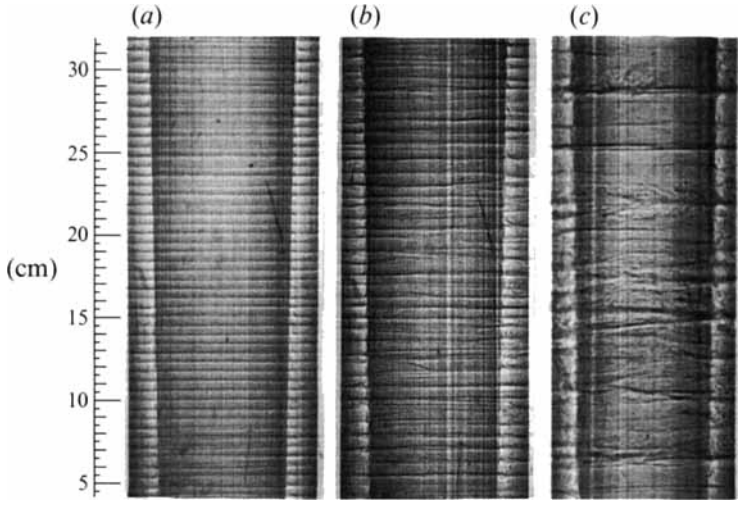

FIGURE 8. Shadowgraph pictures of regular and transition regimes for $N = 1.20\ \mathrm{s}^{-1}$. (*a*) regular S-regime with $\Omega = 0.6\ \mathrm{s}^{-1}$; (*b*) transitian between ST and T-regimes, $\Omega = 0.9\mathrm{s}^{-1}$; (*c*) transition between CT- and STT-regimes, $\Omega = 2.12\ \mathrm{s}^{-1}$.

4. Linear stability analysis

Here we perform a standard linear stability analysis for different values of Reynolds, $Re = \Omega a^2 \epsilon / \nu$, and Froude, $Fr = \Omega / N$, numbers.

4.1. *Governing equations*

In cylindrical coordinates the equations of incompressible stratified flow with uniform viscosity are

$$\frac{\partial u_r}{\partial t} + (\boldsymbol{u}\cdot\nabla)u_r - \frac{u_\varphi^2}{r} = -\frac{1}{\rho_0}\frac{\partial p'}{\partial r} + \nu\left(\Delta u_r - \frac{u_r}{r^2} - \frac{2}{r^2}\frac{\partial u_\varphi}{\partial \varphi}\right), \tag{4.1a}$$

$$\frac{\partial u_\varphi}{\partial t} + (\boldsymbol{u}\cdot\nabla)u_\varphi + \frac{u_r u_\varphi}{r} = -\frac{1}{\rho_0 r}\frac{\partial p'}{\partial \varphi} + \nu\left(\Delta u_\varphi - \frac{u_\varphi}{r^2} + \frac{2}{r^2}\frac{\partial u_\varphi}{\partial \varphi}\right), \tag{4.1b}$$

$$\frac{\partial w}{\partial t} + (\boldsymbol{u}\cdot\nabla)w = -\frac{1}{\rho_0}\frac{\partial p'}{\partial z} - g\frac{\rho'}{\rho_0} + \nu\Delta w, \tag{4.1c}$$

$$\mathrm{div}\ \boldsymbol{u} = 0, \tag{4.1d}$$

$$\frac{\partial \rho'}{\partial t} + w\frac{\mathrm{d}\rho_0}{\mathrm{d}z} = 0, \tag{4.1e}$$

where (u_r, u_φ, w) are the components of velocity respectively in directions (r, φ, z). In (4.1) the Boussinesq approximation has been used with

$$\rho(\boldsymbol{x}) = \rho_0(z) + \rho'. \tag{4.2}$$

In order to reduce the complexity, the density diffusion term in the mass conservation equation has been neglected. This is justified on physical grounds, because in the experiments the Schmidt number is large.

The steady axisymmetric flow solution of (4.1) is

$$u_\varphi^0 = Ar + \frac{B}{r}, \quad u_r^0 = 0, \quad w^0 = 0, \tag{4.3}$$

where

$$A = -\Omega \frac{a^2}{b^2 - a^2} = -\Omega \frac{1}{\mu^2 - 1}, \quad B = -Ab^2 = \Omega a^2 \frac{\mu^2}{\mu^2 - 1}, \quad \mu = \frac{b}{a},$$

and Ω is the angular velocity of the inner cylinder; $u_\varphi^0|_{r=a} = \Omega a$ and the outer cylinder is at rest, $u_\varphi^0|_{r=b} = 0$.

For linear density stratification, $\mathrm{d}\rho_0/\mathrm{d}z = \alpha = \text{const} < 0$, the linearized equations (4.1) for axisymmetric ($\partial/\partial\varphi = 0$) disturbances, periodic in the axial direction

$$(u_r, u_\varphi, w)(r, z, t) = (\tilde{u}_r, \tilde{u}_\varphi, \tilde{w})(r) \mathrm{e}^{\mathrm{i}(\omega t + kz)} \tag{4.4}$$

are

$$\mathrm{i}\omega\tilde{u}_r - 2\left(A + \frac{B}{r^2}\right)\tilde{u}_\varphi = -\frac{\partial}{\partial r}\frac{\tilde{p}}{\rho_0} + \nu\hat{\mathrm{D}}\tilde{u}_r, \tag{4.5a}$$

$$2A\tilde{u}_r + \mathrm{i}\omega\tilde{u}_\varphi = \nu\hat{\mathrm{D}}\tilde{u}_\varphi \tag{4.5b}$$

$$\hat{\mathrm{D}} = \Delta - \frac{1}{r^2}, \tag{4.5c}$$

$$\Delta = \frac{1}{r}\frac{\partial}{\partial r} r \frac{\partial}{\partial r} - k^2, \tag{4.5d}$$

$$\frac{\tilde{p}}{\rho_0} = \frac{1}{k\omega}\left(N^2 - \omega^2 - \mathrm{i}\omega\nu\Delta\right)\tilde{w}, \tag{4.5e}$$

$$\tilde{w} = \frac{\mathrm{i}}{kr}\frac{\partial}{\partial r} r\tilde{u}_r, \tag{4.5f}$$

where the Brunt–Väisälä frequency $N^2 = -(g/\rho_0)(\mathrm{d}\rho_0/\mathrm{d}z) = \text{const}$, and density disturbances were excluded with the help of (4.1*e*). The boundary conditions for the system (4.5) for periodic disturbances with axial wavelength λ are the following:

$$\tilde{u}_\varphi|_{r=a,b} = 0, \quad \tilde{u}_r|_{r=a,b} = 0, \quad \tilde{w}|_{r=a,b} = 0, \quad \tilde{w}|_{z=0,\lambda/2} = 0, \tag{4.6a–d}$$

and from (4.5*f*) the condition $\tilde{w}|_{r=a,b} = 0$ takes the form

$$\frac{\partial \tilde{u}_r}{\partial r} = 0 \ (r = a, b). \tag{4.7}$$

Condition (4.6*d*) gives according to (4.4) $k = 2\pi/\lambda$. Instead of this expression we shall define the wavenumber k by

$$k = \frac{\pi}{nd}, \tag{4.8}$$

where n is the wavelength factor introduced before and $1/n$ corresponds to the number of vortices in a length equal to the gap width ($d = b - a$).

Excluding from (4.5*a*) p/ρ_0 and $\tilde{w}$, we obtain the equation (from hereon we drop the tilde ˜)

$$(\nu\hat{\mathrm{D}} - \mathrm{i}\omega)u_r + 2\left(A + \frac{B}{r^2}\right)u_\varphi = \frac{\partial}{\partial r}\frac{1}{k^2\omega}(N^2 - \omega^2 - \mathrm{i}\omega\nu\Delta)\frac{\mathrm{i}}{kr}\frac{\partial}{\partial r} r u_r,$$

which takes the following form after using (4.5*b*) for u_r:

$$\left[(\nu\hat{\mathrm{D}} - \mathrm{i}\omega)^2 + 4A\left(A + \frac{B}{r^2}\right)\right]u_\varphi = \frac{\mathrm{i}}{k^2\omega}\frac{\partial}{\partial r}(N^2 - \omega^2 - \mathrm{i}\omega\nu\Delta)\frac{1}{r}\frac{\partial}{\partial r} r(\nu\hat{\mathrm{D}} - \mathrm{i}\omega)u_\varphi, \tag{4.9}$$

where

$$\hat{\mathrm{D}} = \frac{\partial^2}{\partial r^2} + \frac{1}{r}\frac{\partial}{\partial r} - \frac{1}{r^2} - k^2.$$

Denoting

$$F = (\nu\hat{\mathrm{D}} - \mathrm{i}\omega)u_\varphi, \quad T = \frac{1}{r}\frac{\partial}{\partial r}rF,$$

we have several relations:

$$\frac{\partial}{\partial r}\frac{1}{r}\frac{\partial}{\partial r}rF = (\hat{\mathrm{D}} + k^2)F, \quad \frac{\partial}{\partial r}\Delta T = (\hat{\mathrm{D}} + k^2)\hat{\mathrm{D}}F.$$

With the help of these relations we finally obtain from (4.9)

$$\left[(\nu\hat{\mathrm{D}} - \mathrm{i}\omega)\hat{\mathrm{D}} + \mathrm{i}\frac{N^2}{\omega}(\hat{\mathrm{D}} + k^2)\right](\nu\hat{\mathrm{D}} - \mathrm{i}\omega)u_\varphi = 4k^2A\left(A + \frac{B}{r^2}\right)u_\varphi \tag{4.10}$$

with the boundary conditions that follow from (4.6), (4.7) and (4.5*b*):

$$u_\varphi|_{r=a,b} = 0, \quad (\nu\hat{\mathrm{D}} - \mathrm{i}\omega)u_\varphi|_{r=a,b} = 0, \quad \frac{\partial}{\partial r}(\nu\hat{\mathrm{D}} - \mathrm{i}\omega)u_\varphi|_{r=a,b} = 0. \tag{4.11}$$

Since $(\nu\hat{\mathrm{D}} - i\omega)u_\varphi = 2Au_r$ it is easy to see that for $N = 0$ this equation transforms to the well-known system (see Di Prima & Swinney 1981) for Couette–Taylor instability.

Introducing the new variables

$$R = (kr)^2, \quad u_\varphi = R^{-1/2}G, \tag{4.12}$$

we obtain the following equation for G (see Appendix A):

$$\mathscr{K}_3\left(R\frac{\mathrm{d}^2}{\mathrm{d}R^2}\right)^3 G + \mathscr{K}_2\left(R\frac{\mathrm{d}^2}{\mathrm{d}R^2}\right)^2 G + \mathscr{K}_1\left(R\frac{\mathrm{d}^2}{\mathrm{d}R^2}\right)G = \mathscr{K}_0 G, \tag{4.13}$$

where

$$\mathscr{K}_3 = \left(4\frac{\nu k^2}{\Omega}\right)^2, \quad \mathscr{K}_2 = -\left(4\frac{\nu k^2}{\Omega}\right)\left(3\frac{\nu k^2}{\Omega} + 2\mathrm{i}\frac{\omega}{\Omega} - \mathrm{i}\frac{N^2}{\omega\Omega}\right),$$

$$\mathscr{K}_1 = \left(\frac{\nu k^2}{\Omega} + \mathrm{i}\frac{\omega}{\Omega}\right)\left(3\frac{\nu k^2}{\Omega} + \mathrm{i}\frac{\omega}{\Omega} - \mathrm{i}\frac{N^2}{\omega\Omega}\right),$$

$$\mathscr{K}_0 = \frac{1}{4(\mu^2-1)^2}\left[4\left(1 - \frac{(ka\mu)^2}{R}\right) + (\mu^2-1)^2\left(\frac{\nu k^2}{\Omega} + \mathrm{i}\frac{\omega}{\Omega}\right)^2\right],$$

with the boundary conditions that follow from (4.11)

$$\left.\begin{aligned} &G|_{R=R_0,R_1} = 0, \quad \frac{\mathrm{d}^2}{\mathrm{d}R^2}G|_{R=R_0,R_1} = 0, \quad R_0 = (ka)^2, \quad R_1 = (kb)^2 = R_0\mu^2, \\ &\frac{\mathrm{d}^3}{\mathrm{d}R^3}G|_{R=R_0,R_1} = \frac{1}{4}\left(1 + \mathrm{i}\frac{\omega}{\nu k^2}\right)\frac{\mathrm{d}}{R\mathrm{d}R}G|_{R=R_0,R_1} = 0. \end{aligned}\right\} \tag{4.14}$$

4.2. *Solutions for the small-gap problem: bounds for inviscid instability*

It is of interest to consider first the inviscid solutions which give lower bounds and a dependence on N. For $\nu = 0$ equation (4.13) becomes

$$4\frac{(N^2 - \omega^2)}{\Omega^2}\frac{\mathrm{d}^2G}{\mathrm{d}R^2} = \left(\frac{4}{(\mu^2-1)^2} - \frac{\omega^2}{\Omega^2} - \frac{4(ka)^2}{R}\frac{\mu^2}{(\mu^2-1)^2}\right)G. \tag{4.15}$$

The first boundary conditions (4.14) are $G = 0$ at $R = R_0, R_1$ (the second conditions are valid according to equation (4.15), and the third conditions that correspond to $w = 0$ on the lateral surfaces of the annulus, $r = a, b$, are not valid for the inviscid case $\nu = 0$).

In terms of the new variable

$$\xi = \frac{b^2 - r^2}{a^2} = \mu^2 - \frac{R}{R_0}, \quad 0 \leqslant \xi \leqslant \mu^2 - 1, \quad R_0 = (ka)^2 = \left(\frac{\pi a}{n(b-a)}\right)^2, \tag{4.16}$$

and in the limit of a small gap

$$\epsilon = \mu - 1 = \frac{b}{a} - 1 \to 0, \tag{4.17}$$

equation (4.15) reduces to

$$\frac{\mathrm{d}^2}{\mathrm{d}\xi^2} G = -\left(\frac{\pi}{n}\right)^2 \frac{\Omega^2}{N^2 - \omega^2} \frac{\xi}{4\epsilon^4} G, \quad G|_{\xi=0;2\epsilon} = 0. \tag{4.18}$$

The solution of (4.18) is

$$G = \xi^{1/2} J_{1/3}(\eta), \quad \eta = \frac{2}{3}\left(\frac{p\xi^3}{4\epsilon^4}\right)^{1/2}, \quad p = \left(\frac{\pi}{n}\right)^2 \frac{\Omega^2}{N^2 - \omega^2}, \tag{4.19}$$

where $J_{1/3}$ is the Bessel function. From the boundary condition at $\xi = 2\epsilon$ it follows that

$$J_{1/3}(\eta_j) = 0, \quad \eta_j = \frac{2}{3}\left(\frac{2p}{\epsilon}\right)^{1/2}. \tag{4.20}$$

For the roots of equation (4.20) we have

$$\eta_1 = 2.9026, \quad \eta_2 = 6.0327. \tag{4.21}$$

For completeness we write the solution for $u_\varphi(r, t)$ which is

$$u_\varphi(r, t) = \frac{\mathrm{e}^{\mathrm{i}\omega t}\left(b^2 - r^2\right)^{1/2}}{kar} J_{1/3}\left(\eta_j \left(\frac{b^2 - r^2}{2\epsilon a^2}\right)^{3/2}\right). \tag{4.22}$$

From this expression it is clear that the root η_1 corresponds to one vortex along the width of the gap, η_2 to two vortices and so on.

From (4.19) and (4.20) we obtain

$$p = \frac{\epsilon}{2}\left(\frac{3\eta_j}{2}\right)^2, \quad \frac{\Omega}{N} = \left(\frac{\epsilon}{2}\right)^{1/2} \frac{3\eta_j n}{2\pi} \frac{1}{\left(1 + \frac{1}{2}\epsilon\left(3\eta_j n/2\pi\right)^2 \omega^2/\Omega^2\right)^{1/2}}$$

and instability for given n with $\omega = -is_r\Omega$ (s_r is real), is possible for

$$\frac{\Omega}{N} = \left(\frac{\epsilon}{2}\right)^{1/2} \frac{3\eta_j n}{2\pi} \frac{1}{\left(1 - \frac{1}{2}\epsilon\left(3\eta_j n/2\pi\right)^2 s_r^2\right)^{1/2}} \geqslant \left(\frac{\epsilon}{2}\right)^{1/2} \frac{3\eta_j n}{2\pi}. \tag{4.23}$$

The bounds corresponding to the right-hand side of (4.23) for $n = \frac{1}{2}$,1, and 2 (approximating the experimentally observed cell sizes) are shown in figure 9 by dash-dotted lines. So, above these lines axisymmetric disturbances with appropriate n are amplified.

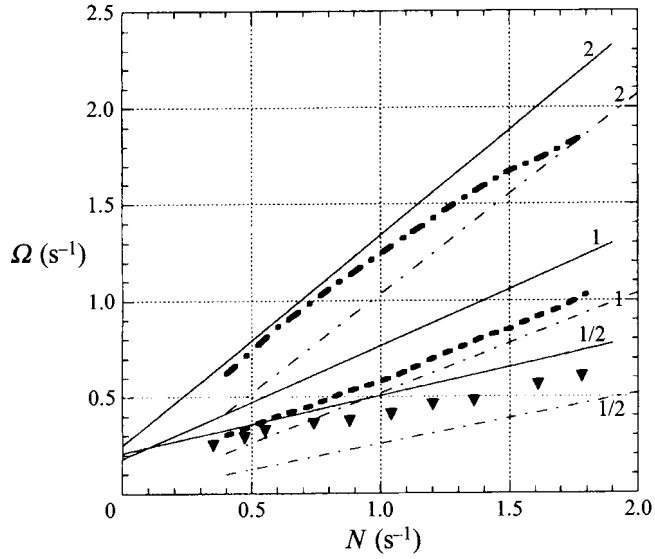

FIGURE 9. Comparison of theoretical and experimental stability bounds (as in figure 1). The theoretical bounds have been calculated for $n = \frac{1}{2}$,1 and 2 (numbers indicated next to the lines); —·—·—, linear, inviscid theory and ——, linear, monotonic viscous theory; ▼, experimental bound of instability onset; - - - and —·— approximate respectively the experimental lower bounds for the existence of Taylor vortices and of compacted vortices.

The amplification rate for given Ω/N is from (4.23)

$$s_r = \left(\frac{2}{\epsilon}\left(\frac{2\pi}{3\eta_j n}\right)^2 - \frac{N^2}{\Omega^2}\right)^{1/2} \tag{4.24}$$

and, hence, for inviscid theory the amplification rate (4.24) is larger for disturbances with small vertical size. It should be emphasized that in the case of $\nu = 0$, for given Ω/N and η_j (4.21), all disturbances with wavenumber factor

$$n \leqslant \frac{\Omega}{N}\left(\frac{2}{\epsilon}\right)^{1/2}\frac{2\pi}{3\eta_j}, \tag{4.25}$$

are amplified. As the cell height tends towards zero ($n \to 0$) the rotation rate for onset of instability would go to zero as well.

Equation (4.20) has the set of solutions η_j and as was noticed from the above solution (4.22), $\eta_j = \eta_1$ describes one vortex pattern across the gap and for $\eta_j = \eta_2$ we have two vortices across. Since $\eta_2/\eta_1 \approx 2$ and, hence, $\eta_1 n \approx \eta_2 n/2$, the bounds of instability (4.23) and the amplification rates (4.24) for vortex patterns with (η_1, n) and $(\eta_2, n/2)$ are approximately the same. So, inviscid instability behaviour of a system with one vortex across and that of a quadruple system (two vortices along one gap height and width) is almost identical.

To finish discussion of inviscid instability theory it is useful to make the following remark about solutions of equation (4.15) without the small-gap assumption. It may be represented in the form

$$\frac{\mathrm{d}^2 G}{\mathrm{d}R^2} = \left(\frac{\theta^2}{4R} + \frac{\vartheta^2 - 1}{4R^2}\right) G,$$

$$\theta^2 = \frac{[4\Omega^2/(\mu^2-1)^2]-\omega^2}{N^2-\omega^2}, \quad \vartheta^2 - 1 = -\frac{4(ka\mu\Omega)^2}{(\mu^2-1)^2(N^2-\omega^2)},$$

$$G = R^{1/2}\left(I_\vartheta(\theta R^{1/2}) + cI_{-\vartheta}(\theta R^{1/2})\right), \quad c = \text{const},$$

where I_q is the modified Bessel function. From boundary conditions for $R = R_0$ and $R = R_1$ it follows that

$$\frac{I_\vartheta(\theta R_0^{1/2})}{I_\vartheta(\theta R_1^{1/2})} = \frac{I_{-\vartheta}(\theta R_0^{1/2})}{I_{-\vartheta}(\theta R_1^{1/2})}, \quad R_0 = (ka)^2, \quad R_1 = (ka\mu)^2.$$

Although this solution is valid for any ϵ, some problems arise when ϵ is small because for this case ϑ becomes imaginary.

4.3. *Viscous monotonic instability and middle-layer approximation*

In terms of the variable

$$\xi = \epsilon x, \quad 0 \leqslant x \leqslant \mu + 1 = 2 + \epsilon, \tag{4.26}$$

instead of (4.16), equation (4.13) and the boundary conditions (4.14), in the limit of $\epsilon \to 0$ take the form

$$K_3\frac{\mathrm{d}^6}{\mathrm{d}x^6}G + K_2\frac{\mathrm{d}^4}{\mathrm{d}x^4}G + K_1\frac{\mathrm{d}^2}{\mathrm{d}x^2}G + K_0 G = 0, \tag{4.27}$$

where

$$K_3 = 64\epsilon\left(\frac{\delta}{\Omega a^2}\right)^2, \quad \delta = \frac{\nu}{\epsilon^2}, \quad K_0 = x\left(\frac{\pi}{n}\right)^2,$$

$$K_2 = 16\mathrm{i}\epsilon\frac{\delta}{\Omega a^2}\left[\frac{N^2-2\omega^2}{\Omega\omega} + 3\mathrm{i}\left(\frac{\pi}{n}\right)^2\frac{\delta}{\Omega a^2}\right],$$

$$K_1 = 4\epsilon\left[\frac{\omega}{\Omega} - \mathrm{i}\left(\frac{\pi}{n}\right)^2\frac{\delta}{\Omega a^2}\right]\left[\frac{N^2-\omega^2}{\Omega\omega} + 3\mathrm{i}\left(\frac{\pi}{n}\right)^2\frac{\delta}{\Omega a^2}\right],$$

$$\left.\begin{aligned} &G|_{x=0,2} = \frac{\mathrm{d}^2}{\mathrm{d}x^2}G|_{x=0,2} = 0, \\ &\frac{\mathrm{d}^3}{\mathrm{d}x^3}G|_{x=0,2} = \left(\frac{\pi}{2n}\right)^2\left(1 + \mathrm{i}\frac{\omega a^2 n^2}{\delta\pi^2}\right)\frac{\mathrm{d}}{\mathrm{d}x}G|_{x=0,2} = 0. \end{aligned}\right\} \tag{4.28}$$

The simplest method to solve the boundary value problem (4.27), (4.28) is to use the middle-layer approximation

$$x \equiv x_0 \approx 1. \tag{4.29}$$

It is worthwhile to point out that this approximation also gives good results for the inviscid case, $\nu = 0$ (see Appendix B).

For constant x (approximation (4.29)) and

$$\frac{\omega}{\Omega} = -\mathrm{i}s_r, \tag{4.30}$$

where s_r is real (and $s_r\Omega > 0$ for instability which is of monotonic type), equation (4.27) and the boundary conditions in (4.28) are real. Solutions of (4.27) can be obtained in the form

$$G = \sum_{i=1}^{6} C_i \mathrm{e}^{k_i x},$$

where k_i, $i = 1, ..., 6$ are the roots (real or complex) of the equation that follows from (4.27). The six boundary conditions (4.28) for $x = 0$ and $x = 2$ give the determinant. By setting the determinant equal to zero we obtain the eigenvalue problem which contains $s_r, \delta, \pi/n, \Omega a^2, N^2/\Omega^2, \epsilon$ as parameters.

On figure 9 the thin solid lines are the neutral stability curves for wavenumber factors $n = \frac{1}{2}, 1, 2$. In the neutral case $N = 0$ the disturbances with $n = 1$ are first amplified if $\Omega > 0.18$. This value corresponds to the expected critical value (for $a/b = 0.8, \Omega_c \approx 0.2$, see Andereck *et al.* 1986). For $N > 0.4$ it is seen from figure 9 that the experimental values for onset of instability and for the bounds of the flow regimes with $n = 1$ and 2 fall between the corresponding theoretical bounds obtained from monotonic viscous and inviscid linear stability solutions.

On figure 10(*a*) the neutral, viscous stability curves are plotted for $n = 1, \frac{2}{3}, \frac{1}{2}, \frac{2}{5}, \frac{1}{3}, \frac{1}{4}$ showing the lower bound of viscous monotonic instability indicated by the dash-dotted envelope curve. This curve is not a linear function of N and even exhibits a minimum slope around $N = 1.2$. The difference between this bound of instability and experiments suggests the existence of an oscillatory or non-axisymmetric instability, as discussed in §3.2, which is the first mode to be amplified.

4.4. *Oscillatory-type instability*

It is well known that in the homogeneous case, $N = 0$, there are no oscillatory instabilities of the azimuthal flow if the outer cylinder is at rest. Even for counter-rotating cylinders oscillatory instabilities are possible for non-axisymmetric modes only (see Demay, Iooss & Laure 1992). Thorpe (1966), using the appropriate results of Chandrasekhar (1961), investigated the oscillatory instability (which in Chandrasekhar is called overstability) for nearly co-rotating cylinders and found that, if the Prandtl number is larger than 1.43, then the critical Taylor number is less than the corresponding value for monotonic instability.

For $N > 0$ we consider the possibility of this type of instability in the asymptotic limit $\nu \to 0$, using equation (4.27) up to the first order in ν (more precisely, the condition of this approximation is $|N^2/\Omega^2 s - 2s| \gg 3\,(\pi/n)^2\,\nu/\epsilon^2\Omega a^2$ for the solution obtained for s (4.38)):

$$\mathscr{A}G + \mathscr{B}\frac{\mathrm{d}^2G}{\mathrm{d}x^2} + \mathscr{C}\frac{\mathrm{d}^4G}{\mathrm{d}x^4} = 0, \tag{4.31}$$

where

$$\mathscr{A} = \left(\frac{\pi}{n}\right)^2 x_0, \quad \delta = \frac{\nu}{\epsilon^2},$$
$$\mathscr{B} = 4\epsilon\left[\frac{N^2}{\Omega^2} + s^2 + \left(\frac{\pi}{n}\right)^2 \frac{\delta}{\Omega a^2}\left(\frac{N^2}{s\Omega^2} + 4s\right)\right],$$
$$\mathscr{C} = -16\epsilon\frac{\delta}{\Omega a^2}\left(\frac{N^2}{s\Omega^2} + 2s\right),$$

with boundary conditions

$$G = \frac{\mathrm{d}^2G}{\mathrm{d}x^2} = 0, \quad x = 0, 2, \tag{4.32}$$

which correspond to $u_\varphi|_{r=a,b} = 0$, $u_r|_{r=a,b} = 0$ and, hence, only conditions $w|_{r=a,b} = 0$ are not fulfilled at this order in ν.

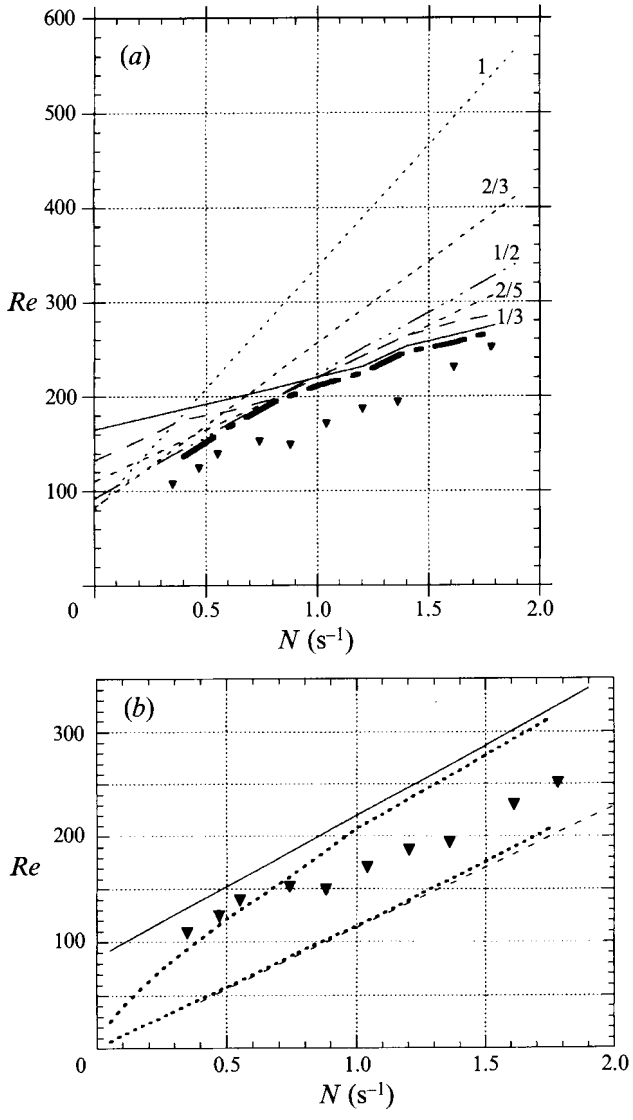

FIGURE 10. (*a*) Neutral stability bounds in the (*Re*,*N*) plane for vortices with wavelength factors $n = 1, \frac{2}{3}, \frac{1}{2}, \frac{2}{5}, \frac{1}{3}, \frac{1}{4}$; ▼, experimental bound of instability onset; —— · —— · —— · ——, envelope curve for monotonic instability with the most unstable wavenumbers. (*b*) Region (between dotted lines) of oscillatory-type instability in the (*Re*,*N*) plane for $n = \frac{1}{2}, j = 1$; – – –, linear, inviscid theory and ——, linear, monotonic viscous theory for $n = \frac{1}{2}$; ▼, experimental bound of instability onset; $Re = \Omega a(b-a)/\nu$.

Multiplying (4.31) by $\mathrm{d}^2G^*/\mathrm{d}x^2$ and integrating by parts from 0 to 2 subject to (4.32), we obtain (G^* is complex conjugate of G):

$$\mathscr{B}I_2 - \mathscr{A}I_1 - \mathscr{C}I_3 = 0,$$

$$(\mathscr{B} + \mathscr{B}^*)I_2 - (\mathscr{C} + \mathscr{C}^*)I_3 = 2\mathscr{A}I_1, \tag{4.33}$$

$$(\mathscr{B} - \mathscr{B}^*)I_2 = (\mathscr{C} - \mathscr{C}^*)I_3, \tag{4.34}$$

where

$$\left.\begin{aligned} &I_1 = \int_0^2 |G'|^2\,\mathrm{d}x,\quad I_2 = \int_0^2 |G''|^2\,\mathrm{d}x,\quad I_3 = \int_0^2 |G'''|^2\,\mathrm{d}x,\\ &\mathscr{B} - \mathscr{B}^* = (s-s^*)\,4\epsilon\left[s+s^* + \frac{\delta}{\Omega a^2}\left(\frac{\pi}{n}\right)^2\left(4 - \frac{N^2}{\Omega^2|s|^2}\right)\right],\\ &\mathscr{C} - \mathscr{C}^* = -(s-s^*)\,16\epsilon\frac{\delta}{\Omega a^2}\left(2 - \frac{N^2}{\Omega^2|s|^2}\right). \end{aligned}\right\} \tag{4.35}$$

It follows from (4.34) and (4.35) that

$$(s-s^*)\left\{\left[(s+s^*)\frac{\Omega a^2}{\delta} + \left(\frac{\pi}{n}\right)^2\left(4 - \frac{N^2}{\Omega^2|s|^2}\right)\right] I_2 + 4\left(2 - \frac{N^2}{\Omega^2|s|^2}\right) I_3\right\} = 0. \tag{4.36}$$

This equation may be valid if:

(i) $s = s^*$; in this case there are no oscillations, the growth or decay of disturbances is monotonic;

(ii) $s \neq s^*$; in this case we have

$$s + s^* = -\frac{\delta}{\Omega a^2}\left[\left(\frac{\pi}{n}\right)^2\left(4 - \frac{N^2}{\Omega^2|s|^2}\right) + 4\left(2 - \frac{N^2}{\Omega^2|s|^2}\right)\frac{I_3}{I_2}\right]. \tag{4.37}$$

If here, $N = 0$, then $s + s^* < 0$ (further we put $\Omega > 0$). This means that oscillations ($\mathrm{Im}(s) \neq 0$) in the non-stratified case could exist only in the steady Taylor–Couette regime ($\mathrm{Re}(s) < 0$). So, for instability it is necessary that $N > 0$. From (4.37) and (4.33) in the limit $\delta \to 0$ for unstable solution ($s + s^* > 0$) we obtain (see Appendix C)

$$s = s_r + \mathrm{i}s_i,\quad 2s_r = s + s^* \approx \left(\frac{x_0}{4\epsilon}\left(\frac{\pi}{n}\right)^2\frac{I_1}{I_2} - \frac{N^2}{\Omega^2}\right)^{1/2}, \tag{4.38}$$

$$s_r^2 + s_i^2 = |s|^2 \approx \frac{\delta}{\Omega a^2}\,\frac{N^2}{\Omega^2}\,\frac{(\pi/n)^2 + 4I_3/I_2}{\left(\dfrac{x_0}{4\epsilon}\left(\dfrac{\pi}{n}\right)^2\dfrac{I_1}{I_2} - \dfrac{N^2}{\Omega^2}\right)^{1/2}}. \tag{4.39}$$

The condition

$$s_r^2 + s_i^2 \geqslant s_r^2, \tag{4.40}$$

gives from (4.38),(4.39) the bounds of this type of instability in the form:

$$\frac{\delta}{\Omega a^2}\,\frac{N^2}{\Omega^2}\left[\left(\frac{\pi}{n}\right)^2 + 4\frac{I_3}{I_2}\right] \geqslant \frac{1}{4}\left[\frac{x_0}{4\epsilon}\left(\frac{\pi}{n}\right)^2\frac{I_1}{I_2} - \frac{N^2}{\Omega^2}\right]^{3/2}. \tag{4.41}$$

Now we shall use for the integrals I_1, I_2 and I_2 in (4.41) the middle-layer, inviscid approximation (B 2) (see Appendix B) having in mind that (4.41) also was obtained for the limit $v \to 0$. So, from (B 2),(B 3) we have

$$\frac{I_1}{I_2} = \left(\frac{2}{\pi j}\right)^2,\quad \frac{I_3}{I_2} = \left(\frac{\pi j}{2}\right)^2,$$

where πj is the non-dimensional radial wavenumber, and the inequality (4.41) gives (for $x_0 = 1$)

$$\left[\frac{1}{\epsilon}\left(\frac{1}{nj}\right)^2 - \frac{N^2}{\Omega^2}\right]^{3/2} \leqslant \frac{4\pi^2\delta}{\Omega a^2}\,\frac{N^2}{\Omega^2}\left[\left(\frac{1}{n}\right)^2 + j^2\right]. \tag{4.42}$$

From (4.38) and (4.42) equation (B 4) follows indicating that (4.42) extends into the region of inviscid instability ($\nu \to 0$), and is close to the bound of this instability (for given wavelength factor n).

According to (4.40), if we have equality in (4.42) then $s_i = 0$. In the case of strong inequality (4.42) we obtain oscillatory-type instability, $s_i \neq 0$. From (4.38) the amplification rate s_r of this instability, $e^{i\omega t} = e^{s_r \Omega t + i s_i \Omega t}$, is equal to

$$s_r \approx \frac{1}{2}\left(\frac{1}{\epsilon}\left(\frac{1}{nj}\right)^2 - \frac{N^2}{\Omega^2}\right)^{1/2}. \tag{4.43}$$

By comparison with (B 4) it is interesting to note that the amplification rate of this oscillatory instability is half the amplification rate of inviscid monotonic instability for the same external parameters $N, \Omega, \epsilon, n, j$.

On figure 10(b) the lower and upper bounds of oscillatory instability given by (4.42) are shown for $n = \frac{1}{2}$, $j = 1$ and $\nu = 0.01$ cm^{2}s^{-1}. The experimental values (curve a in figure 1) lie within these bounds. Of course, this value of ν cannot be considered as asymptotically small and the regions on figure 10(b) are some approximation of real conditions. From (4.43) it follows that the amplification rates (s_r) for one vortex pattern in the layer of height half the gap width, $n = \frac{1}{2}, j = 1$ and for a quadruple vortex pattern in this layer, $n = \frac{1}{4}, j = 2$, are equal (within the precision of the middle-layer approximation). But, the frequencies of oscillations for this system of vortices s_i are different. From (4.39) and (4.43) we obtain for $n = \frac{1}{2}, j = 1$, $s_i^{(1)} = \left[(\delta/\Omega a^2)(N^2/\Omega^2)(5\pi^2/2s_r) - s_r^2\right]^{1/2}$ and for $n = \frac{1}{4}, j = 2$, $s_i^{(1)} = \left[(\delta/\Omega a^2)(N^2/\Omega^2)(20\pi^2/2s_r) - s_r^2\right]^{1/2}$. Hence, for given Ωa^2 and N/Ω, $s_i^{(2)} > s_i^{(1)}$. This means that the period of oscillation for a small-scale vortex pattern, $T_2 = 2\pi/s_i^{(2)}$, is less than for one vortex across the gap, $T_1 = 2\pi/s_i^{(1)}$ (at least $T_1 > 2T_2$).

Asuming that these systems of vortices exist simultaneously, we can imagine the following picture of oscillations (figure 11). During some time ($T \leqslant T_1/2$) when one vortex keeps some definite direction of rotation (figure 11a), the vortices in the quadruple arrangement change their direction of rotation (figure 11b). This results in a structure with different positions of maximum-vorticity region (figure 11c).

The change of direction of rotation of the one-vortex system with the period T_1 produces some modulation of the oscillations. This would be one of the possible mechanisms to explain, in the framework of an axisymmetric velocity field, the periodicity which is observed experimentally near onset of instability (figure 4). In §3.2 it was mentioned that the instability near onset is actually non-axisymmetric. The above quadruple system of vortices may be non-axisymmetrically unstable because of the presence of a saddle point between the vortices. In the case of counter-rotating homogeneous Couette–Taylor flow non-axisymmetric oscillatory instability is also found to occur at lower critical Reynolds number than monotonic instability, but the difference between the critical Reynolds numbers is very small (see Demay *et al.* 1992).

5. Discussion and conclusions

The main result of the experiments is the formation of layers in the stratified fluid with their height taking on discrete values instead of changing in a continuous fashion with Ω. For the configuration considered, the smallest layer height is less than the gap width between the cylinders and is about half the gap width at small N, decreasing

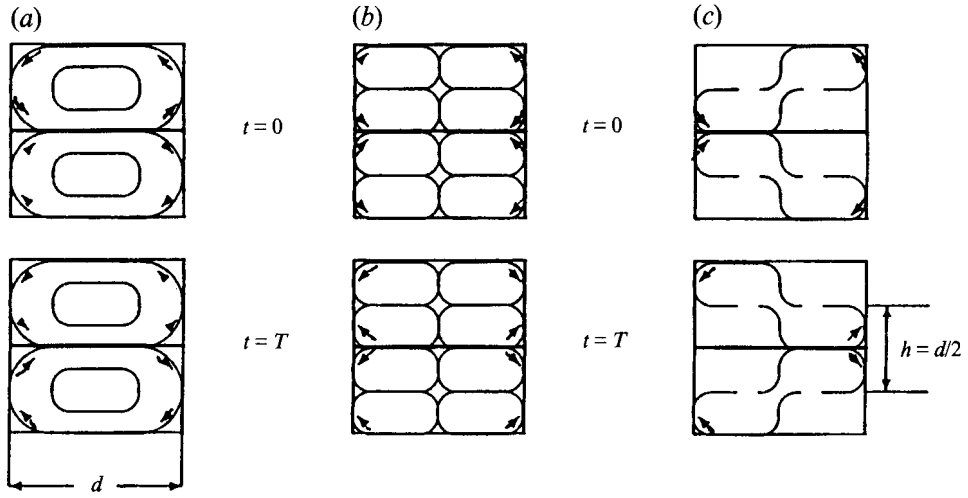

FIGURE 11. Schematic representation of oscillations in the vortex system for (*a*) $n = \frac{1}{2}, j = 1$ and (*b*) $n = \frac{1}{4}, j = 2$ (b); (*c*) is the resulting vortex pattern due to interaction of (*a*) and (*b*) configurations.

with increasing N. The origin for this layer formation is the mixing caused by the vortex structures resulting from the most amplified wavelength at different values of (Ω, N). Near onset of instability the most amplified mode has a wavelength factor of $n \approx 1/2$ and the instability is non-axisymmetric. Linear stability theory indicates that the most unstable mode is of oscillatory type, possibly non-axisymmetric. At larger values of Ω modes $n = 1$ and $n = 2$ are successively amplified. The azimuthal secondary instability observed in homogeneous fluid is suppressed by stratification. Internal waves are, however, generated. Their influence on the dynamics of the flow is secondary because, generally, the energy contained in these waves is a small fraction of the energy in the coherent vortex structures. In the viscous theory internal wave motion is one solution which has not been looked for.

The experiments are conducted with a fluid at large Schmidt number (about 10^3) and it is, therefore, justified to neglect density diffusion in the mass conservation equation. For lower Prandtl number (order 1) the discrete mode selection still exists (Orlandi 1994) but stable density layers could, probably, only form if the Péclet number is large, $Pe = uh/\kappa \gg 1$, where u is a characteristic velocity of the vortices and κ the diffusivity. For Prandtl number less than about 1.43 the instability is monotonic (Thorpe 1966) but this does not noticeable affect the height of the rolls.

The experiments have been conducted bearing in mind the possible relevance of the results to equatorial jet formation. Measurements by Firing (1987) in the meridional plane show isovelocities which give the image of flattened cells of aspect ratio (width to height) of about 300. The largest aspect ratio in the present experiments is 2 to 3 only. The question is whether a larger gap and larger Reynolds number would give larger aspect ratios. Experiments with a larger gap but similar Reynolds numbers as in the present experiments indeed show an increase in aspect ratio (Boubnov, Gledzer & Hopfinger 1994).

The dependence of the aspect ratio on Reynolds number and gap width may be deduced from energy arguments. The simplest one is to consider that some part of the kinetic energy of a fluid element near the inner cylinder, $E \sim (a\Omega)^2/2$, transforms

into potential energy $\mathscr{P} \sim g(\rho'/\rho_0)(h/2)$ when it is elevated by some height h resulting in a density change $\rho' \sim |\mathrm{d}\rho_0/\mathrm{d}z|h$. So $E \geqslant \mathscr{P}$ gives

$$(a\Omega)^2 \geqslant \frac{g}{\rho_0}\left|\frac{\mathrm{d}\rho_0}{\mathrm{d}z}\right|h^2$$

or

$$\frac{h}{d} \leqslant \frac{\Omega}{\epsilon N}. \tag{5.1}$$

This differs from inviscid, linear stability theory which shows that

$$\frac{h}{d} \leqslant \frac{\Omega}{k_i \epsilon^{1/2} N}, \quad k_i = \frac{3\eta_i}{8^{1/2}\pi}, \quad k_1 = 0.98, \quad k_2 = 2.04 \tag{5.2}$$

(k_1 corresponds to a one-vortex pattern along the gap width, k_2 to two vortices). To improve the energy arguments, consider a fluid particle which moves near the outer trajectory of the vortex of width d and height h (for a toroidal vortex this corresponds to some thin circular vortex ring which changes its radius). For Couette flow the centrifugal force u_φ^2/r is balanced by the appropriate pressure gradient directed toward the inner cylinder. When the particle moves toward the outer cylinder the centrifugal force produces work. If the value of the centrifugal force is taken equal to $a\Omega^2$ (near the inner cylinder), then at the distance d the corresponding work is equal to $W = da\Omega^2$. The work done during elevation of a fluid element by height h is $W = g|\rho'/\rho_0|h = N^2h^2$. This gives an estimation for the maximum value of h for given Ω/N by setting

$$da\Omega^2 \geqslant N^2h^2, \quad \frac{h}{d} \leqslant \frac{\Omega}{\epsilon^{1/2}N}. \tag{5.3}$$

This differs only slightly from (5.2) for $i = 1$.

It is now possible to include in the previous considerations the influence of viscous forces. According to Navier–Stokes equations the viscous force is $\nu\pi^2\left(2/d^2 + 1/h^2\right)a\Omega$ for a one-vortex pattern across the gap. The corresponding additional work is $\nu\pi^2\left(2/d^2 + 1/h^2\right)a\Omega\left(d^2/2 + h^2\right)^{1/2}$ giving the relation

$$da\Omega^2 \sim N^2h^2 + \nu\pi^2\left(\frac{2}{d^2} + \frac{1}{h^2}\right)a\Omega\left(d^2/2 + h^2\right)^{1/2}, \tag{5.4}$$

which describes the balance between centrifugal, buoyancy and viscous forces. The term $d^2/2$ in (5.4) was taken to describe the fact that for $N = 0$ the minimum rotation Ω_m is for Taylor vortices with $d \approx h$ (minimum of the right-hand side of (5.4) with $N = 0$) and is equal to $\Omega_m = (\nu/a^2\epsilon^2)\pi^2 3(\frac{3}{2})^{1/2} \sim 0.2$ for $a = 4$ cm, $\epsilon \sim 0.3$.

With increasing N the minimum of Ω is realized for values $h_m < d$. For large enough N the following approximations are obtained from (5.4):

$$\frac{h_m}{d} \sim \left(\frac{\nu\pi^2}{Na^2\epsilon^{5/2}}\right)^{1/3}, \quad \frac{\Omega_m}{N} \sim \sqrt{2}\left(\frac{\nu\pi^2}{Na^2\epsilon}\right)^{1/3}. \tag{5.5}$$

From (5.5) for $a = 4$ cm, $\epsilon = 0.275$ we obtain for $N = 0.5$, $h_m/d \approx 0.7$ and for $N = 1$, $h_m/d \approx 0.5$ in accordance with the experimental results of §3.2. The values of the minimum layer height h_m and minimum angular velocity Ω_m at onset of instability are related by

$$\frac{h_m}{d} \sim \frac{1}{(2\epsilon)^{1/2}}\frac{\Omega_m}{N}. \tag{5.6}$$

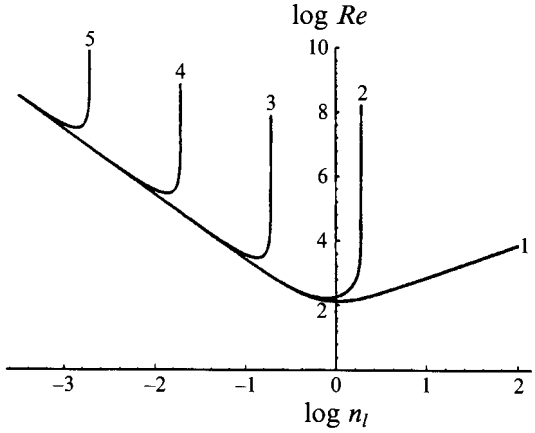

FIGURE 12. Relation between Re and layer height factor $n_l = h/d$ for (1) $Fr = \infty$; (2) $Fr = 1$; (3) $Fr = 10^{-1}$; (4) $Fr = 10^{-2}$; (5) $Fr = 10^{-3}$, calculated from equation (5.7).

For $\epsilon = 0.275$ we obtain $1/(2\epsilon)^{1/2} \approx 1.35$ which is very close to the experimental value given by (3.1).

From equation (5.4) follows the relation between Reynolds number $Re = \Omega ad/\nu$ and layer height factor $n_l = h/d$ for given Froude number Fr:

$$Re = \frac{\pi^2(1+2n_l^2)^{3/2}}{\epsilon n_l^2\sqrt{2}} \frac{1}{1-\epsilon n_l^2/Fr^2}. \tag{5.7}$$

In figure 12 this relation is shown for different Froude numbers demonstrating a decrease in n_l with increasing Reynolds number and decreasing Froude number Fr. In the equatorial ocean $Fr \sim 10^{-3}$, $n_l \sim \frac{1}{300}$, which gives $Re \sim 10^7$ when $\epsilon \sim 1$. The velocity of the undercurrent (below the main thermocline) is typically $U \sim 0.5$ m s^{-1} and the halfwidth $d \sim 100$ km. This gives an eddy viscosity $\nu_t \sim 10^{-3}$ m^2 s^{-1}, which is an upper bound of the (vertical) eddy viscosity usually taken in numerical models of tropical oceans (Pacanowski & Philander 1981). In these models a turbulent Prandtl number, $Pr_t = \nu_t/\kappa_t$, of about 10 is used which can still be considered large. As discussed above, even a turbulent Prandtl number of 1 would not make the experimental results and the theoretical analysis inapplicable because the height of the rolls is hardly altered when $Pr \to 1$ (Orlandi 1994) and nearly constant density layers of height h could still form, due to mixing by the rolls, if $d/U \ll h^2/\kappa_t$.

The authors wish to thank Bach Lien Hua who was at the origin of this work. Many discussions with her during the course of the research were also most valuable. This research has been financially supported by grant IFREMER No 93-2-424151 LPO. E. B. Gledzer was supported by DRET (contract 93-1100) and B. M. Boubnov held a visiting Professor position at the INPG.

Appendix A

We intend to represent (4.10), (4.11) in variables (4.12). For $\hat{\mathrm{D}}$ the following relation is valid:

$$\hat{\mathrm{D}} = k^2\hat{\mathrm{d}}, \quad \hat{\mathrm{d}} = 4\frac{\partial}{\partial R}R\frac{\partial}{\partial R} - \frac{1}{R} - 1,$$

Instead of (4.10) we obtain:

$$\left((\nu k^2\hat{\mathrm{d}} - \mathrm{i}\omega)k^2\hat{\mathrm{d}} + \mathrm{i}\frac{N^2}{\omega}k^2(\hat{\mathrm{d}}+1)\right)(\nu k^2\hat{\mathrm{d}} - \mathrm{i}\omega)u_\varphi = 4k^2A\left(A + \frac{Bk^2}{R}\right)u_\varphi. \tag{A 1}$$

With the help of relations

$$(\hat{\mathrm{d}}+1)u_\varphi = 4R^{1/2}\frac{\mathrm{d}^2G}{\mathrm{d}R^2}$$

the following representation of equation (A 1)

$$\left(\hat{P}(\hat{\mathrm{d}}+1) - \hat{P} + \mathrm{i}\frac{N^2}{\omega\Omega}(\hat{\mathrm{d}}+1)\right)\hat{P}u_\varphi = 4\frac{1}{(\mu^2-1)^2}\left(1 - \frac{(ka\mu)^2}{R}\right)u_\varphi,$$

$$\hat{P} = \frac{\nu k^2}{\Omega}(\hat{\mathrm{d}}+1) - \left(\frac{\nu k^2}{\Omega} + \mathrm{i}\frac{\omega}{\Omega}\right)$$

is transformed to

$$\left(4\hat{\pi}R\frac{\mathrm{d}^2}{\mathrm{d}R^2} - \hat{\pi} + 4\mathrm{i}\frac{N^2}{\omega\Omega}R\frac{\mathrm{d}^2}{\mathrm{d}R^2}\right)\hat{\pi}G = 4\frac{1}{(\mu^2-1)^2}\left(1 - \frac{(ka\mu)^2}{R}\right)G,$$

$$\hat{\pi} = \left[\frac{4\nu k^2}{\Omega}R\frac{\mathrm{d}^2}{\mathrm{d}R^2} - \left(\frac{\nu k^2}{\Omega} + \mathrm{i}\frac{\omega}{\Omega}\right)\right],$$

which gives (4.13).

Appendix B

We have from (4.27) or (4.18)

$$\frac{\mathrm{d}^2}{\mathrm{d}x^2}G + \left(\frac{\pi}{n}\right)^2\frac{\Omega^2}{N^2-\omega^2}\frac{x}{4\epsilon}G = 0. \tag{B 1}$$

If we use the approximation (4.29) in the second term in (B 1), then the solution is

$$G = \sin\left(\frac{\pi}{2n}\frac{\Omega}{(N^2-\omega^2)^{1/2}}\frac{1}{\epsilon^{1/2}}x\right) \tag{B 2}$$

The boundary condition $G|_{x=2} = 0$ gives

$$\frac{\pi}{2n}\frac{\Omega}{(N^2-\omega^2)^{1/2}}\frac{1}{\epsilon^{1/2}} = \frac{\pi j}{2},\quad j = 1, 2, 3, \ldots,\quad \frac{1}{n} = \frac{d}{h},$$

$$\frac{\Omega}{N} = \left(\frac{\epsilon}{2}\right)^{1/2}\frac{\sqrt{2}jn}{\left(1 + \frac{1}{2}\epsilon\left(\sqrt{2}jn\right)^2\omega^2/\Omega^2\right)^{1/2}}, \tag{B 3}$$

and instability $\omega^2 = -s_r^2\Omega^2$ for the inviscid middle-layer approximation exists, with corresponding amplification rate s_r, if

$$\frac{\Omega}{N} \geqslant \epsilon^{1/2}jn,\quad s_r = \left(\frac{2}{\epsilon}\left(\frac{1}{\sqrt{2}jn}\right)^2 - \frac{N^2}{\Omega^2}\right)^{1/2}. \tag{B 4}$$

Here, $j = 1$ describes one vortex across the gap, $j = 2$ two vortices and so on. For $j = 1$ the factor $\sqrt{2} \approx 1.41$ in (B 3), (B 4) replaces the value $3\eta_1/2\pi \approx 1.38$ in (4.24), (4.23).

Appendix C

From (4.37) we have

$$|s|^2 = \frac{N^2}{4\Omega^2} \frac{(\pi/n)^2 + 4I_3/I_2}{\frac{1}{4}(s+s^*)(\Omega a^2/\delta) + (\pi/n)^2 + 2I_3/I_2}. \tag{C 1}$$

Equation (4.33) has the form

$$2x_0 \left(\frac{\pi}{n}\right)^2 I_1 = 4\epsilon \left[2\frac{N^2}{\Omega^2} + s^2 + (s^*)^2 + \left(\frac{\pi}{n}\right)^2 \frac{\delta}{\Omega a^2}(s+s^*)\left(4 + \frac{N^2}{\Omega^2|s|^2}\right)\right] I_2$$

$$+ 16\epsilon \frac{\delta}{\Omega a^2}(s+s^*)\left(2 + \frac{N^2}{\Omega^2|s|^2}\right) I_3, \tag{C 2}$$

Now let us consider the limit $\delta \to 0$. Equation (C 1) becomes

$$|s|^2 \approx \frac{\delta}{\Omega a^2} \frac{1}{s+s^*} \frac{N^2}{Q\Omega^2}, \quad Q = \frac{1}{(\pi/n)^2 + 4I_3/I_2} \tag{C 3}$$

Using $s^2 + (s^*)^2 = (s+s^*)^2 - 2|s|^2$ and (C 3) we have instead of (C 2)

$$2x_0 \left(\frac{\pi}{n}\right)^2 I_1 \approx 4\epsilon \left(2\frac{N^2}{\Omega^2} + (s+s^*)^2 + \left(\frac{\pi}{n}\right)^2 Q(s+s^*)^2\right) I_2 + 16\epsilon Q(s+s^*)^2 I_3$$

$$= 8\epsilon I_2 \left(\frac{N^2}{\Omega^2} + (s+s^*)^2\right).$$

From this, for the unstable solution ($s + s^* > 0$), equation (4.38) is obtained, and also (C 3) gives equation (4.39).

REFERENCES

ALI, M. & WEIDMAN, P. D. 1990 On the stability of circular Couette flow with radial heating. *J. Fluid Mech.* **220**, 53–84.

ANDERECK, C. N., LIU, S. S. & SWINNEY, H. L. 1986 Flow regimes in a circular Couette system with independently rotating cylindes. *J. Fluid Mech.* **164**, 155–183.

BOUBNOV, B. M., GLEDZER, E. B. & HOPFINGER, E. J. 1994 Layer formation in stratified circular Couette flow. In *Preprints Fourth Intl Symp. on Stratified Flows*, vol. 2.

CHANDRASEKHAR, S. 1961 *Hydrodynamics and Hydromagnetic Stability*. Oxford University Press.

CHOOSSAT, P. & IOOSS, G. 1994 The Couette-Taylor problem. In *Appl. Math. Sci.* **102**.

COOPER, E. R., JANKOWSKI, D. F., NEITZEL, G. P. & SQUIRE, T. H. 1985 Experiments on the onset of instability in unsteady Couette flow. *J. Fluid Mech.* **161**, 97–114.

COUETTE, M. 1890 Études sur le frottement des liquides. *Ann. Chim. Phys.* **21**, 433.

DEMAY, Y., IOOSS, G. & LAURE, P. 1992 Wave patterns in the small gap Couette-Taylor problem. *Eur. J. Mech.* B/*Fluids* **11**, 621–634.

DI PRIMA, R. C. & SWINNEY, H. L. 1981 Instabilities and transition in flow between concentric rotating cylinders. In *Hydrodynamic Instability and the Transition to Turbulence* (ed. H. L. Swinney & J. P. Collub). Topics in Applied Physics, vol. 45, pp. 139–180. Springer.

FIRING, E. J. 1987 Deep zonal currents in the central equatorial Pacific. *J. Mar. Res.* **45**, 791.

GRAVAS, N. & MARTIN, B.W. 1978 Instability of viscous axial flow in annuli having a rotating inner cylinder. *J. Fluid Mech.* **86**, 385–394.

HUA, B. L. & MOORE, D. W. 1994 Inertial stability of subthermocline equatorial flows. *Annales Geophysicae* (2), **12**(Suppl.) , C221.

KUBOTANI, H., MIYAMA, S. M., SEKIYA, M. & KOJIMA, Y. 1989 The surface wave instability of stratified incompressible cylinders with differential rotation. *Prog. Theor. Phys.* **82**, 523–534.

LUEPTOV, R. M., DOCTER, A. & MIN, K. 1992 Stability of axial flow in an annulus with a rotating inner cylinder. *Phys. Fluids* A **4**, 2446–2455.

ORLANDI, P. 1994 Stratified Taylor-Couette flow: numerical simulation. In *Preprints Fourth Intl Symp. on Stratified Flows*, vol. 2.

OSTER, G. 1965 Density gradients. *Sci. Am.* **213**, 70–76.

PACANOWSKY, R. C. & PHILANDER, S. G. H. 1981 Parametrization of vertical mixing in numerical models of tropical oceans. *J. Phys. Oceanogr.* **11**, 1443–1451.

SNYDER, H. A. & KARLSSON, S. K. 1964 Experiments on the stability of Couette motion with a radial thermal gradient. *Phys. Fluids* **7**, 1696–1706.

TAYLOR, G. I. 1923 Stability of a viscous fluid contained between two rotating cylinders. *Phil. Trans. R. Soc. Lond.* A **233**, 289–343.

THORPE, S. A. 1966 The stability of stratified Couette flow. In *Notes on 1966 Summer Geophys. Fluid Dyn.* Woods Hole Oceanographic Inst. pp. 80–107.

VERONIS, G. 1970 The analogy between rotating and stratified fluids. *Ann. Rev. Fluid Mech.* **2**, 37–66.

YAO, L. S. & ROGERS, B. B. 1989 The linear stability of mixed convection in a vertical annulus. *J. Fluid Mech.* **201**, 279–298.